

# Inferring Optical Depth of Broken Clouds above Green Vegetation Using Surface Solar Radiometric Measurements

HOWARD W. BARKER

*Environment Canada, Downsview, Ontario, Canada*

ALEXANDER MARSHAK

*NASA Goddard Space Flight Center, Greenbelt, Maryland*

(Manuscript received 3 August 2000, in final form 14 February 2001)

## ABSTRACT

A method for inferring cloud optical depth  $\tau$  is introduced and assessed using simulated surface radiometric measurements produced by a Monte Carlo algorithm acting on fields of broken, single-layer, boundary layer clouds derived from Landsat imagery. The method utilizes a 1D radiative transfer model and time series of zenith radiances and irradiances measured at two wavelengths,  $\lambda_1$  and  $\lambda_2$ , from a single site with surface albedos  $\alpha_{\lambda_1} < \alpha_{\lambda_2}$ . Assuming that clouds transport radiation in accordance with 1D theory and have spectrally invariant optical properties, inferred optical depths  $\tau'$  are obtained through cloud-base reflectances that are approximated by differencing spectral radiances and estimating upwelling fluxes at cloud base. When initialized with suitable values of  $\alpha_{\lambda_1}$ ,  $\alpha_{\lambda_2}$ , and cloud-base altitude  $h$ , this method performs well at all solar zenith angles. Relative mean bias errors for  $\tau'$  are typically less than 5% for these cases. Relative variances for  $\tau'$  for given values of inherent  $\tau$  are almost independent of inherent  $\tau$  and are  $<50\%$ . Errors due to neglect of net horizontal transport in clouds yield slight, but systematic, overestimates for  $\tau \leq 5$  and underestimates for larger  $\tau$ . Frequency distributions and power spectra for retrieved and inherent  $\tau$  are often in excellent agreement. Estimates of  $\tau$  depend weakly on errors in  $h$ , especially when  $h$  is overestimated. Also, they are almost insensitive to errors in surface albedo when  $\alpha_{\lambda_1}$  is underestimated and  $\alpha_{\lambda_2}$  overestimated. Reversing the sign of these errors leads to overestimation of  $\tau$ , particularly large  $\tau$ . In contrast, the conventional method of using only surface irradiance yields almost entirely invalid results when clouds are broken.

Though results are shown only for surfaces resembling green vegetation (i.e.,  $\alpha_{\lambda_1} \ll \alpha_{\lambda_2}$ ), the performance of this method depends little on the values of  $\alpha_{\lambda_1}$  and  $\alpha_{\lambda_2}$ . Thus, if radiometric data have sufficient signal-to-noise ratios and suitable wavelengths can be found, this method should yield reliable estimates of  $\tau$  for broken clouds above many surface types.

## 1. Introduction

Cloud optical depth  $\tau$  plays an important role in determining the radiation budgets of the earth's surface and atmosphere. Thus, it is essential that global climate models produce realistic spatial and temporal distributions of  $\tau$ . The best way to verify these distributions is to infer  $\tau$  from global coverage satellite data (Rossow and Schiffer 1991; Han et al. 1998). There can, however, be many sources of uncertainty and error with these methods so independent and reliable estimates of  $\tau$  are essential for validation (e.g., Min and Harrison 1996; Li et al. 1999). Due largely to minimal cost, inference of  $\tau$  from solar radiometric observations made at the surface is the obvious candidate for meeting this need.

One way to estimate  $\tau$  from the surface is to use direct-beam transmittances. However, a sun tracker is required, multiple forward scattering must be accounted for, and the upper limit of inferred  $\tau$  is rather small and inversely proportional to the cosine of solar zenith angle  $\theta_0$ . The most common method for inferring  $\tau$  from the surface involves broadband irradiances measured by pyranometers. Using estimated input parameters and exploiting the 1-to-1 relation between  $\tau$  and surface irradiance  $F^\downarrow$  for plane-parallel, homogeneous atmospheres above uniform surfaces (see Fig. 1),  $\tau$  are usually obtained via precomputed tables (Leontyeva and Stamnes 1994; Leontyeva et al. 1994; Barker et al. 1998).

A major limitation with the pyranometer method is that it works well for overcast conditions only, and even then retrieved  $\tau$  are *effective* values for the pyranometer's field of view (FOV). While narrow FOV zenith radiances  $I^\downarrow$  measured at the surface avoid this problem, Fig. 1 shows that  $I^\downarrow$  does not enjoy the 1-to-1 relation

---

*Corresponding author address:* Dr. Howard Barker, Cloud Physics Research Division (ARMP), Meteorological Service of Canada, 4905 Dufferin St., Downsview, ON M3H 5T4, Canada.  
E-mail: howard.barker@ec.gc.ca

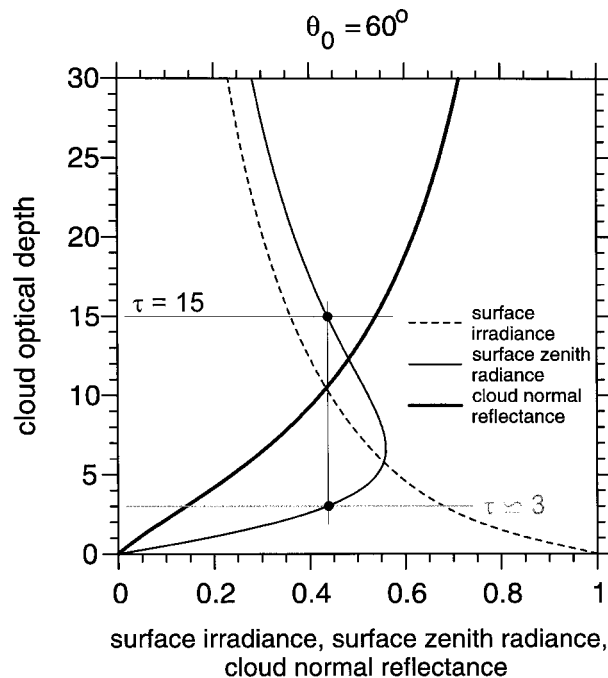


FIG. 1. Cloud optical depth  $\tau$  as a function of surface irradiance and surface zenith radiance for solar zenith angle  $\theta_0 = 60^\circ$ , and cloud-normal reflectance for isotropic irradiance as computed by the 1D radiative transfer algorithm DISORT (Stamnes et al. 1988). Cloud normal reflectance is defined as the fraction of isotropic irradiance that is reflected normal to the cloud. Sixteen streams, the Henyey–Greenstein phase function, cloud droplet asymmetry parameter and single-scattering albedo of 0.85 and 1.0, and a surface albedo of 0.2 were used in DISORT. Take, e.g., a cloud of  $\tau = 15$ . It would produce unambiguous values of surface irradiance and cloud normal reflectance of  $\sim 0.35$  and  $\sim 0.55$ , respectively. Likewise, it would produce a zenith radiance of  $\sim 0.43$  but so too would a cloud of  $\tau \approx 3$ . If only radiances were available, one could not decide on the correct root. As shown later, when conditions are less than ideal (i.e., realistic), establishing unambiguous roots from zenith radiances and surface irradiances can often be expected to be impossible; when normal reflectances can be isolated, they are much more reliable.

with  $\tau$  that  $F^\downarrow$  does. But, as also shown in Fig. 1, the relation between  $\tau$  and the component of  $I^\downarrow$  made up of photons that are multiply reflected between surface and cloud is again 1-to-1. Thus, if this component of  $I^\downarrow$  could be isolated, it might be possible to estimate  $\tau$  in a narrow FOV at zenith.

With this in mind, Marshak et al. (2000) defined a Normalized Difference Cloud Index (NDCI) as

$$\text{NDCI} \equiv \frac{I_{\lambda_2}^\downarrow - I_{\lambda_1}^\downarrow}{I_{\lambda_2}^\downarrow + I_{\lambda_1}^\downarrow}, \quad (1)$$

where  $I_\lambda^\downarrow$  are measured at two wavelengths  $\lambda$ . Ideally, conditions at  $\lambda_1$  and  $\lambda_2$  are as follows: very similar cloud optical properties, minimal attenuation by other atmospheric constituents, and, surface albedo at  $\lambda_2$  is much larger than at  $\lambda_1$ . As pointed out by Marshak et al., green vegetated surfaces often satisfy these conditions for  $\lambda_1 \approx 0.65 \mu\text{m}$  and  $\lambda_2 \approx 0.85 \mu\text{m}$  where surface albedos are typically  $< 0.1$  and  $> 0.4$  due to a rapid

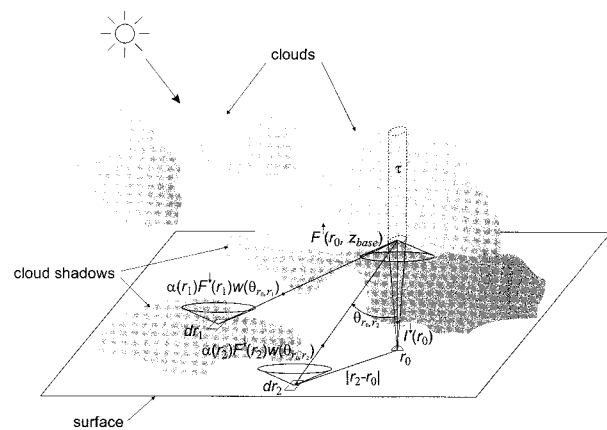


FIG. 2. Schematic diagram showing that cloud-base irradiance  $F^\uparrow(r_0, z_{\text{base}})$  at  $r_0$  is made up of photons reflected by the surface at points  $r$  with albedo  $\alpha(r)$  and irradiance  $F^\downarrow(r)$ , which are, in turn, tied to cloud structure. The fraction of photons reflected by the surface that make it to  $r_0$  on cloud base is defined by  $w$ . The fraction of photons in  $F^\uparrow(r_0, z_{\text{base}})$  that emerge from  $r_0$  depends on optical depth  $\tau$  above  $r_0$ . Ultimately,  $I^\downarrow(r_0)$  is measured at the surface.

decline in absorption by chlorophyll (see Table 1). Basically, the numerator of (1) attempts to isolate photons in  $I_\lambda^\downarrow$  that have been reflected by the surface. The remaining step, however, is to go from NDCI to  $\tau$ . Marshak et al. hypothesized that this method may work for nonovercast conditions.

The purpose of the present paper is to present and test a new method of inferring  $\tau$  for inhomogeneous clouds using surface-based radiometric observations. This method was motivated by Marshak et al.’s NDCI but instead of using an index, it is physically based

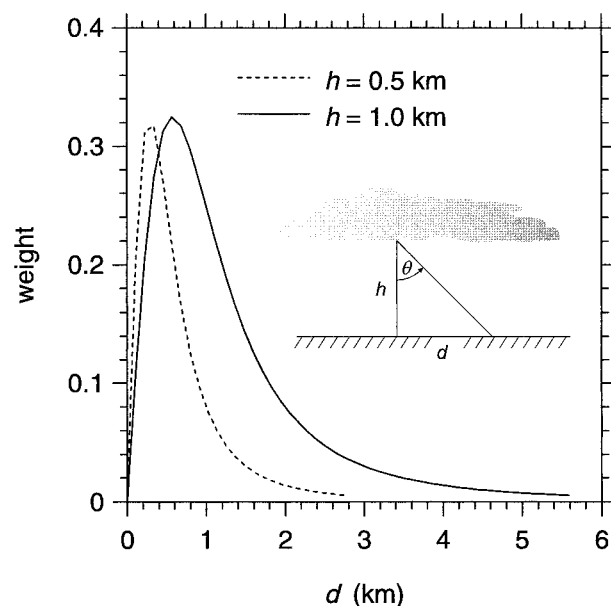


FIG. 3. Weighting function as defined in (11a) for two values of cloud-base altitude  $h$  as functions of distance  $d$  where  $d = h \tan(\theta)$  as shown in the plot [see (11b)]. Both curves terminate at  $\theta = 80^\circ$ .

TABLE 1. Some examples of visible (VIS) and near-infrared (NIR) surface albedos (Kimes 1983; Kimes et al. 1986; Myneni and Asrar 1993; Lyapustin 1999).

Surface type	VIS	NIR
Irrigated wheat	0.06	0.44
Grasses	0.03	0.45
Hardwood forest	0.04	0.31
Coniferous forest	0.06	0.42
Black spruce	0.02	0.17
Leaf forest	0.05	0.48
Savannah	0.03	0.55
Wheat	0.07	0.55
Plowed field	0.17	0.18
Loam	0.25	0.33

and requires spectral surface irradiances in addition to zenith radiances. The theoretical foundation and application algorithm of this method are presented in section 2. As radiometric measurements were simulated for this study, the 3D Monte Carlo radiative transfer algorithm and its input fields are discussed in section 3. Results are presented in section 4, and section 5 contains conclusions.

## 2. Model development

This part contains three sections. The first presents a Green's function-based formulation of zenith radiances as measured at the surface along with the assumptions and simplifications that make for a tractable model. The second describes how upwelling irradiance at cloud base is estimated using time series of measured surface irradiance. In the third, some operational considerations are described. Hereinafter, all radiometric quantities are assumed to be normalized by spectral irradiance at some level above cloud top. Moreover, it is assumed that the atmosphere is transparent between surface and cloud, and that surface radiometric observations are made close to the ground at a single location.

### a. Theoretical background

Consider zenith radiance  $I^\downarrow(r_0)$  measured at  $r_0$  on the surface. Photons comprising  $I^\downarrow$  can be partitioned into those that have not encountered the surface  $I^0(r_0)$  and those that have any number of times. Following Knyazikhin and Marshak (2000), for a Lambertian surface,  $I^\downarrow$  can be expressed as

$$I^\downarrow(r_0) = I^0(r_0) + \int_{\mathcal{R}} F^\uparrow(r) \mathcal{G}(|r_0 - r|) dr, \quad (2)$$

where  $F^\uparrow$  is upwelling flux at  $r \in \mathcal{R}$  on the surface,  $\mathcal{G}$  is a Green's, or influence, function that describes the fraction of  $F^\uparrow$  at  $r$  that is redirected by droplet scattering into the sensor at  $r_0$ . In general,  $\mathcal{G}$  will vary due both to cloud structure and surface radiance patterns. As shown later,  $I^0$  depends intractably on solar zenith angle

$\theta_0$  and cloud structure and is what NDCI and the model developed here try to avoid.

If the atmosphere is overcast and homogeneous and the surface uniform and Lambertian (i.e., ideal 1D conditions),  $F^\uparrow$ , radiance distributions, and the integral of  $\mathcal{G}$  are all independent of  $r$  and (2) becomes

$$I^\downarrow(r_0) = I^0(r_0) + F^\uparrow(r_0) \int_{\mathcal{R}} \mathcal{G}_{pp}(|r_0 - r|) dr, \quad (3)$$

for all  $r_0$  where  $\mathcal{G}_{pp}$  is the Green's function for a plane-parallel cloud. On the other hand, conventional 1D theory (e.g., Box et al. 1988) would define  $I^\downarrow$  as

$$\begin{aligned} I^\downarrow &= I^0 + T\alpha\rho_\tau + T\alpha^2\alpha_\tau\rho_\tau + T\alpha^3\alpha_\tau^2\rho_\tau + \dots \\ &= I^0 + \left( \frac{\alpha T}{1 - \alpha\alpha_\tau} \right) \rho_\tau = I^0 + F^\uparrow \rho_\tau, \end{aligned} \quad (4)$$

where  $\alpha$  is surface albedo,  $T$  is cloud transmittance for collimated irradiance (i.e., surface irradiance when  $\alpha = 0$ ), and  $\rho_\tau$  and  $\alpha_\tau$  are cloud-base reflectance into nadir and spherical albedo given uniform, isotropic illumination (the subscript  $\tau$  signifies dependence on  $\tau$  only). Equating (3) and (4) implies that

$$\rho_\tau = \int_{\mathcal{R}} \mathcal{G}_{pp}(|r_0 - r|) dr, \quad (5)$$

which relates 3D transfer to the conventional 1D solution. Though these simplified conditions do not apply in a 3D atmosphere, a simplified version of (2), which borrows much from the 1D solution, is constructed here.

Returning to more general conditions, first multiply and divide the last term in (2) by the integral of  $\mathcal{G}$  over  $\mathcal{R}$ . Then, assume that for the integral of  $\mathcal{G}$  in the numerator: (i) all upwelling fluxes are isotropic; and (ii) to first-order approximation, radiation is transported locally through clouds in accordance with 1D theory (cf. the independent pixel approximation; Cahalan et al. 1994; Barker 1996a; Marshak et al. 1999). This enables (2) to be approximated as

$$I^\downarrow(r_0) \approx I^0(r_0) + \left\{ \int_{\mathcal{R}} F^\uparrow(r) \left[ \frac{\mathcal{G}(|r_0 - r|)}{\int_{\mathcal{R}} \mathcal{G}(|r_0 - r'|) dr'} \right] dr \right\} \rho_\tau(r_0), \quad (6)$$

where  $\rho_\tau(r_0)$  depends now only on  $\tau$  above  $r_0$ , and the term in square brackets can be considered as a normalized Green's function. In keeping with the 1D approximation, if effective upwelling irradiance onto cloud base at  $r_0$  is defined as

$$F^\uparrow(r_0, z_{\text{base}}) \equiv \int_{\mathcal{R}} F^\uparrow(r) \left[ \frac{\mathcal{G}(|r_0 - r|)}{\int_{\mathcal{R}} \mathcal{G}(|r_0 - r'|) dr'} \right] dr, \quad (7)$$

(6) becomes

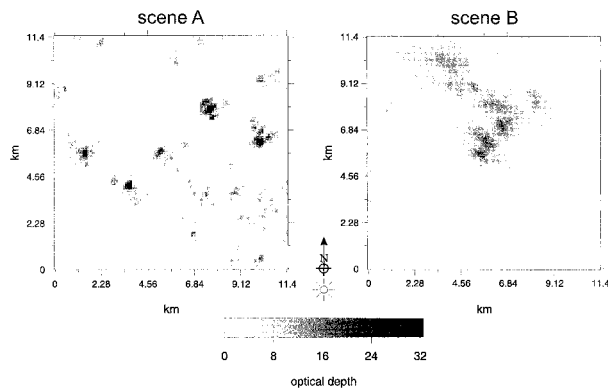


FIG. 4. Cloud optical depth inferred from Landsat imagery for two single layer, marine boundary layer cloud fields (see Table 2 for scene information). In all simulations the Sun shown in from the bottom of the plot (i.e., from the south as indicated).

$$I^\downarrow(r_0) \approx I^0(r_0) + F^\uparrow(r_0, z_{\text{base}})\rho_\tau(r_0), \quad (8)$$

which is similar to (4) and used hereinafter to approximate  $I^\downarrow(r_0)$ .

The approximations made here reduce  $\mathcal{G}$  to a pale semblance of its true self, as its control over explicit radiative transfer is restricted by  $\rho_\tau$ . In actuality,  $\mathcal{G}$  could be viewed as having two components: one describing photon trajectories from surface to cloud, and another describing photon trajectories once inside clouds. By virtue of a transparent atmosphere below cloud, the former component is a pure geometric translation (each point on the surface feeding all points on cloud base) and is addressed partially in the next section. The latter component has been studied for planar (homogeneous and fractal) clouds by Davis et al. (1997). An exploration of  $\mathcal{G}$  when sources are removed from cloud boundaries is beyond the scope of this study. Also, the high rate of sampling errors expected with a single set of radiometers warrants only a simple representation of  $\mathcal{G}$  as used in the next section where an approximation for  $F^\uparrow(r_0, z_{\text{base}})$  is developed.

#### b. Estimating upwelling irradiance at cloud base

The underlying hypothesis of the procedure presented in this section is that single time series of surface irradiance contain sufficient information about area-average surface irradiance (i.e., cloud structure) to make accurate estimates of cloud-base irradiance in the zenith. As such, if one had a full 2D description of downwelling surface irradiance  $F^\downarrow$ ,  $F^\uparrow$  at cloud base could be expressed as

$$F^\uparrow(r_0, z_{\text{base}}) = \frac{\int_{\mathcal{R}} \alpha(r) F^\downarrow(r) w(\theta_{r_0, r}) dr}{\int_{\mathcal{R}} w(\theta_{r_0, r}) dr}, \quad (9)$$

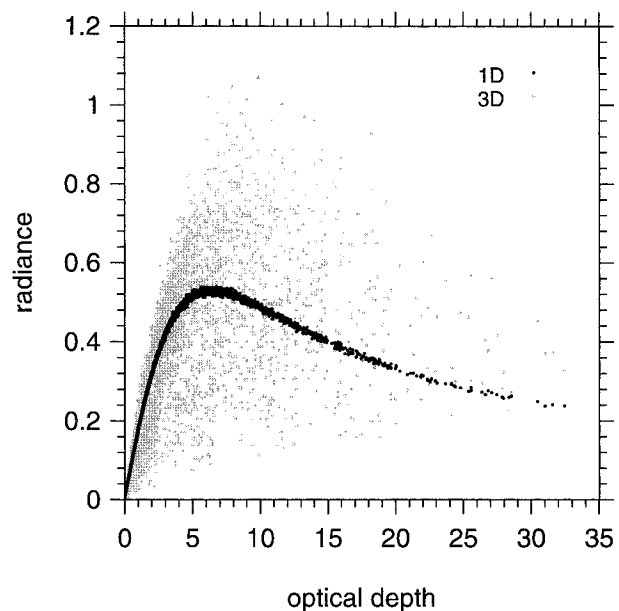


FIG. 5. Zenith radiances as a function of cloud optical depth for  $\theta_0 = 60^\circ$  when underlying surface is black [ $I^0$  in (2), (3), (4), and (8)]. These were computed by the Monte Carlo algorithm in 1D and 3D mode for scene A. The scatter of points for 1D transfer indicates Monte Carlo noise.

where  $w$  is a weighting function (which is similar to a surface bidirectional reflectance distribution function and when normalized approximates normalized  $\mathcal{G}$ ) that depends on distance between  $r$  on the surface and  $r_0$  on cloud base (directly above  $r_0$  on the surface) and the zenith angle  $\theta_{r_0, r}$  formed between that line and the normal to the surface at  $r_0$ . Figure 2 shows a schematic depiction of (9). The procedure developed here assumes that only one surface site exists, and that constant, local-average surface albedos  $\langle \alpha \rangle$  are adequate. Therefore, making the frozen turbulence assumption and using  $n$  measured irradiances either side of  $F^\downarrow(j)$ ,  $F^\uparrow$  in the zenith at the time of the  $j^{\text{th}}$  measurement is approximated by

$$F^\uparrow(j, z_{\text{base}}) \approx \langle \alpha \rangle \frac{\sum_{k=j-n}^{j+n} F^\downarrow(k) w(k-j)}{\sum_{k=j-n}^{j+n} w(k-j)}. \quad (10)$$

If the surface is pointwise Lambertian, the contribution to  $F^\uparrow(j, z_{\text{base}})$  from a unit area source at  $k$  on the surface depends inversely on the square of the distance between the points and directly on projected area of the source. Therefore,  $w$  is proportional to  $\cos^3 \theta_{j,k}$  where  $\theta_{j,k}$  is nadir angle between the  $j^{\text{th}}$  point on cloud base and the  $k^{\text{th}}$  point on the surface [i.e.,  $\theta_{r_0, r}$  in (9)]. Assuming further that  $F^\downarrow(k)$  represents the mean of the annulus on which it sits, concentric about  $j$ , an additional factor of  $\sin \theta_{j,k}$  enters, and a reasonable form of  $w$  is

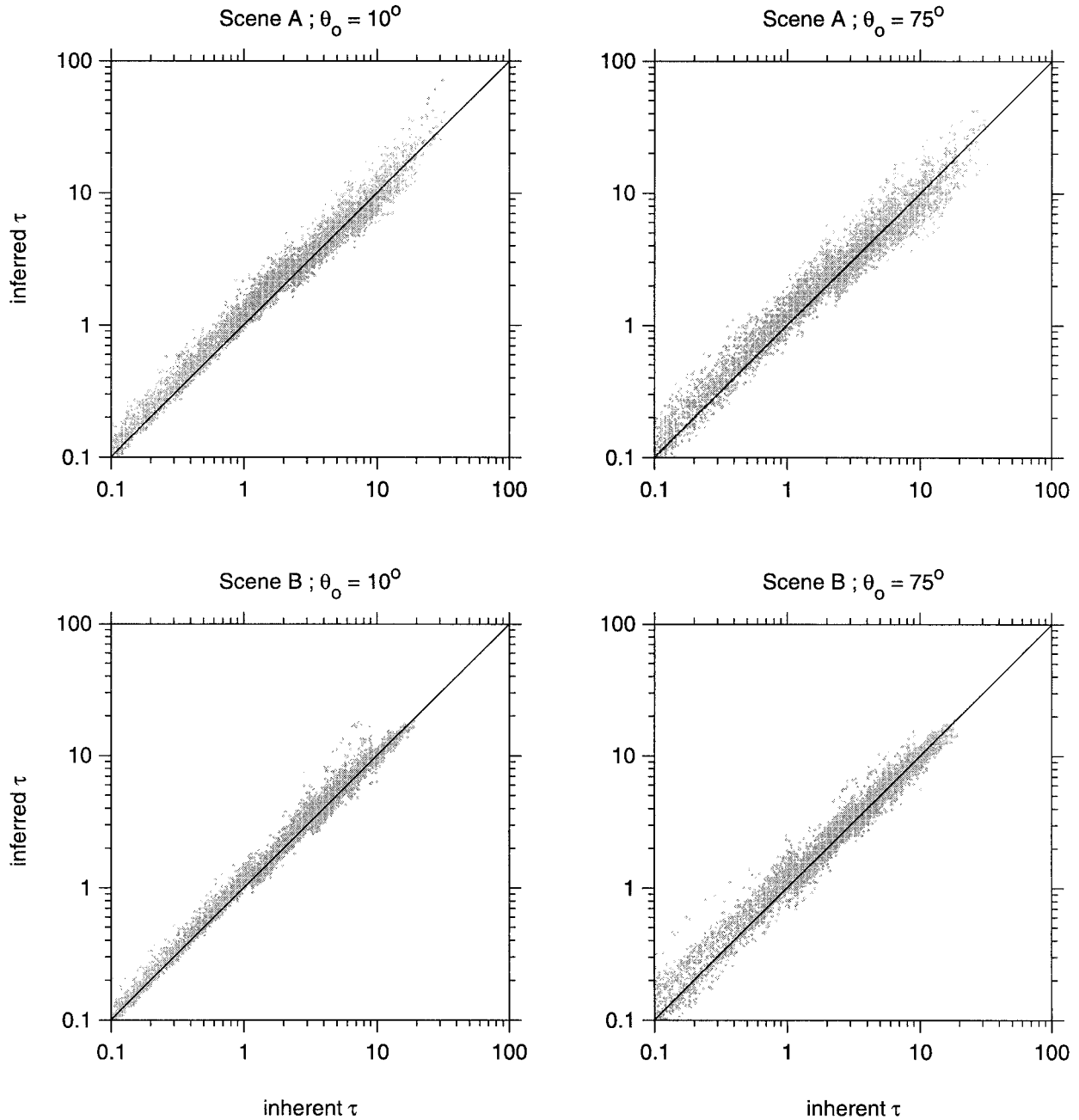


FIG. 6. Inferred  $\tau$  plotted against inherent  $\tau$  for scenes A and B at two values of  $\theta_0$ . Inferred values correspond to transects parallel to the Sun.

$$w(k - j) = \cos^3 \theta_{j,k} \sin \theta_{j,k}. \tag{11a}$$

In practice,  $\theta_{j,k}$  could be approximated as

$$\theta_{j,k} = \tan^{-1} \left( \frac{|k - j| |\mathbf{v}| \Delta t}{h} \right), \tag{11b}$$

where  $|\mathbf{v}|$  is cloud advection rate,  $\Delta t$  is measurement integration period, and  $h$  is cloud-base altitude. When working with regular grids of simulated measurements, as was the case here,  $|\mathbf{v}| \Delta t$  equals horizontal grid spac-

ing (or multiples thereof). Figure 3 shows examples of  $w$  as defined in (11a).

Two simple limiting situations for the weighting function in (10) deserve mention. First, if  $w(k - j) \equiv \delta_{kj}$ , where

$$\delta_{kj} = \begin{cases} 0; & k \neq j \\ 1; & k = j, \end{cases}$$

only instantaneous irradiance at  $j$  is used to estimate

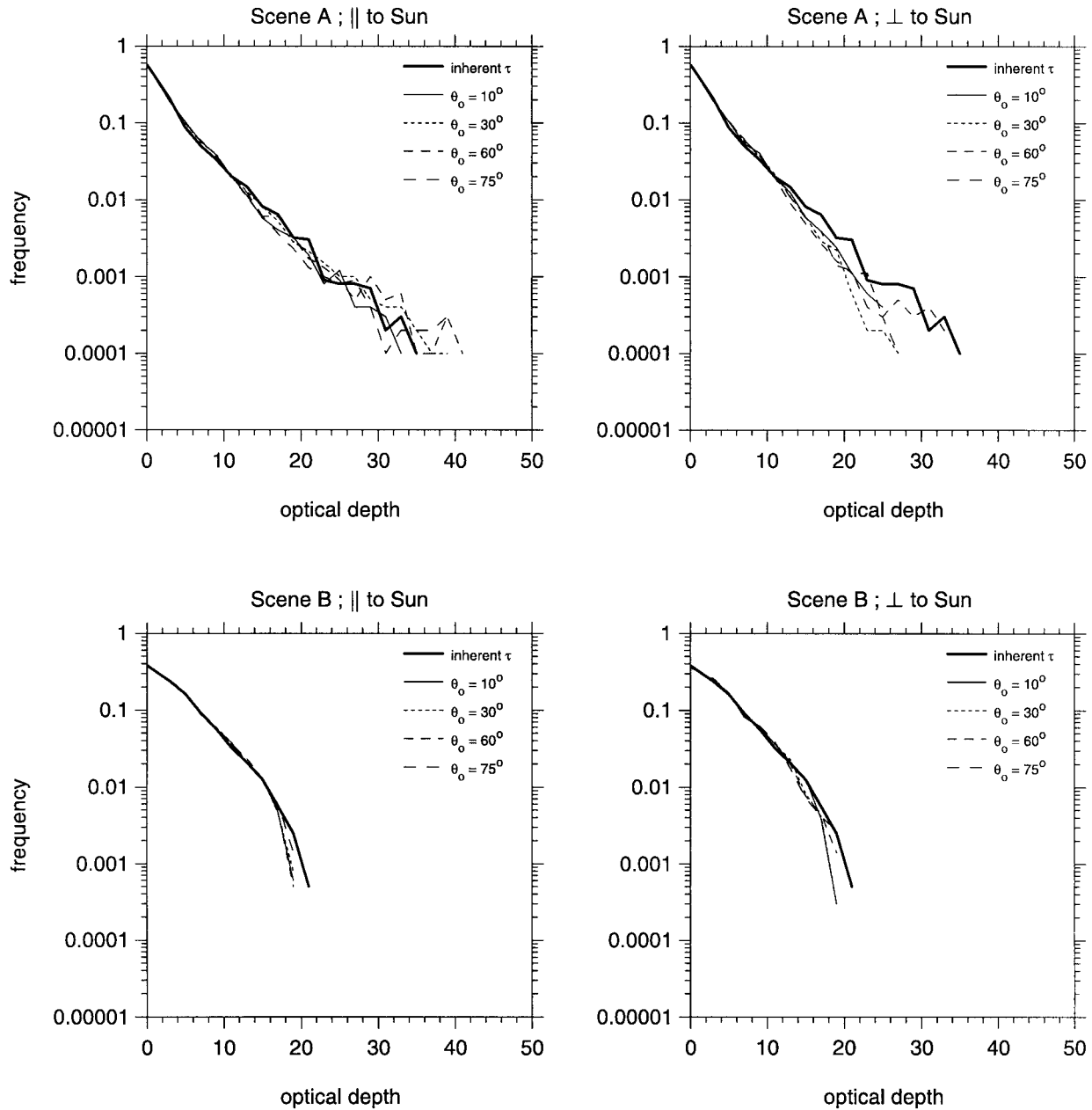


FIG. 7. (top) Frequency distributions (bin width = 1) of inherent  $\tau$  and corresponding  $\tau'$  at several  $\theta_0$  for scene A. Distributions of  $\tau'$  are concatenations of values retrieved along all 100 transects parallel to ( $\parallel$ ) and perpendicular to ( $\perp$ ) the Sun. (bottom) Same as (top) expect they are for scene B.

$F^\uparrow(j, z_{\text{base}})$ . Second, if  $w(k-j)$  is constant, all measured irradiances along a times series are given equal weight in determining  $F^\uparrow(j, z_{\text{base}})$ .

### c. Spectral differencing and operational details

Assume now that surface measurements of zenith radiance and irradiance are available at two wavelengths,  $\lambda_1$  and  $\lambda_2$ , that have essentially equal atmospheric optical properties but  $\langle \alpha \rangle_{\lambda_1} < \langle \alpha \rangle_{\lambda_2}$ . This means that  $I^\downarrow$ ,

$I^0$ , and  $\rho_\tau$  in (8) are common to both wavelengths, but  $F_{\lambda_1}^\uparrow < F_{\lambda_2}^\uparrow$ . Thus, evaluating (8), using (10), for both sets of spectral measurements, differencing them and rearranging, one obtains

$$\rho_\tau(j) = \frac{I_{\lambda_2}^\downarrow(j) - I_{\lambda_1}^\downarrow(j)}{F_{\lambda_2}^\uparrow(j, z_{\text{base}}) - F_{\lambda_1}^\uparrow(j, z_{\text{base}})}, \quad (12)$$

where the offending quantity  $I^0$  has been eliminated [as in Marshak et al.'s (2000) NDCI].

All that is required now is to find  $\tau$  needed to produce

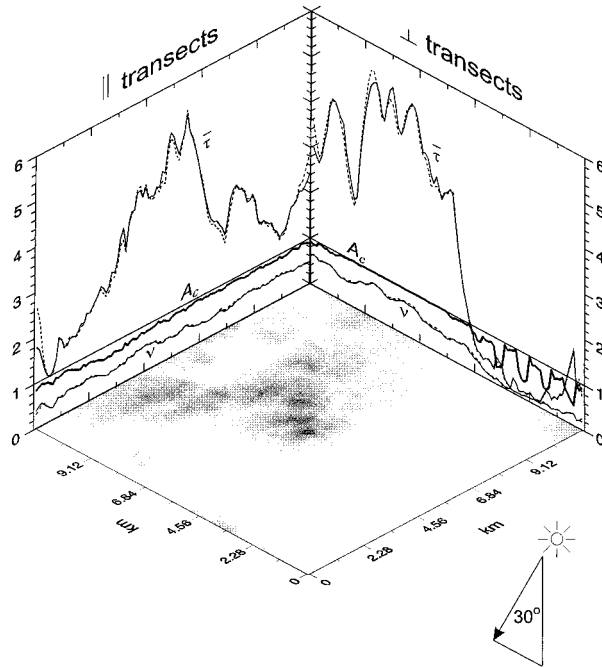


FIG. 8. Curves running along edges of the map of scene B show inherent (thin solid lines) and inferred (thin dotted lines) values of mean optical depth  $\bar{\tau}$  and  $\nu \equiv (\bar{\tau})^2/\bar{\tau}^2$  for each transect either parallel to ( $\parallel$ ) or perpendicular to ( $\perp$ ) incoming sun. In this case,  $\theta_0 = 30^\circ$ . Heavy solid lines are vertically projected cloud fraction  $A_c$  along each transect (horizontal solid line of value 1 denotes overcast).

estimated cloud reflectance  $\rho_\tau$ . This was done by running the 16-stream version of DISORT (Stamnes et al. 1988) with the Henyey–Greenstein phase function (Henyey and Greenstein 1941) at asymmetry parameter  $g = 0.85$  for 14 values of  $\tau$ . For each  $\tau$ , DISORT was run twice: with a black surface ( $\alpha = 0$ ) and a white surface ( $\alpha = 1$ ). Making use of (4),  $\rho_\tau$  can be solved for as

$$\rho_\tau = \frac{I_{\alpha=1}^\downarrow(\tau) - I_{\alpha=0}^\downarrow(\tau)}{F_{\alpha=1}^\downarrow(\tau)}. \quad (13)$$

Using the 14 ordered pairs of  $(\tau, \rho_\tau)$ , the Padé approximant

$$\tau' = \frac{\sum_{m=0}^6 a_m \rho_\tau^m}{\sum_{m=0}^7 b_m \rho_\tau^m}, \quad (14)$$

was created where  $a_m$  and  $b_m$  are coefficients. This fit is accurate to within about  $\pm 0.5\%$  for  $\tau$  between 0.01 and 100. Alternatively, one could employ DISORT in a root-finding algorithm. Thus, estimates of  $\tau$  are obtained by evaluating the rhs of (12) and substituting for  $\rho_\tau$  in (14). Hereinafter, estimates of  $\tau$  are denoted as  $\tau'$ . A second method to be used when only radiances are measured is presented in the appendix.

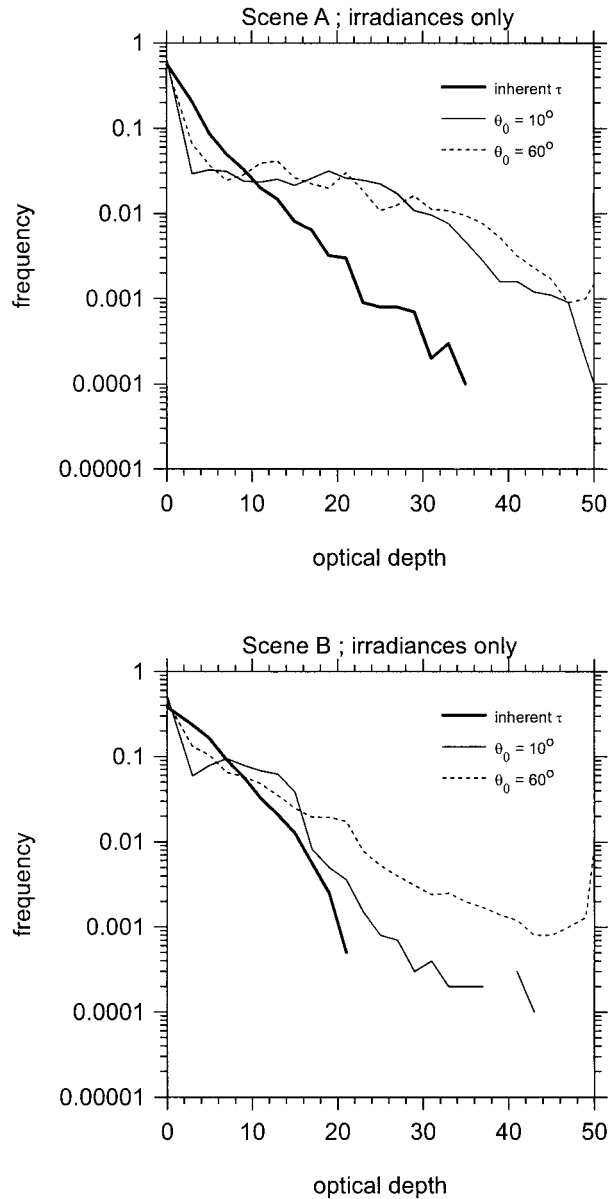


FIG. 9. Frequency distributions (bin width = 1) of inherent  $\tau$  and  $\tau'$  estimated by the traditional method that uses only surface irradiance (e.g., Leontieva and Stamnes 1994). These results are for scenes A and B at  $\theta_0 = 10^\circ$  and  $60^\circ$  (cf. results in Fig. 7).

### 3. Simulating radiometric measurements and cloud data

A 3D Monte Carlo photon transport algorithm employing cyclic horizontal boundary conditions was used to compute  $F_\lambda^\downarrow$  and narrow field of view  $I_\lambda^\downarrow$  via the local estimation method (Marchuk et al. 1980). The Henyey–Greenstein phase function with  $g = 0.85$  was used to represent scattering by nonabsorbing cloud droplets. Aerosols were neglected as was Rayleigh scattering since the entire atmosphere's molecular optical depth at  $\lambda \approx 0.7 \mu\text{m}$  is just  $\sim 0.04$ . Ground surfaces were as-

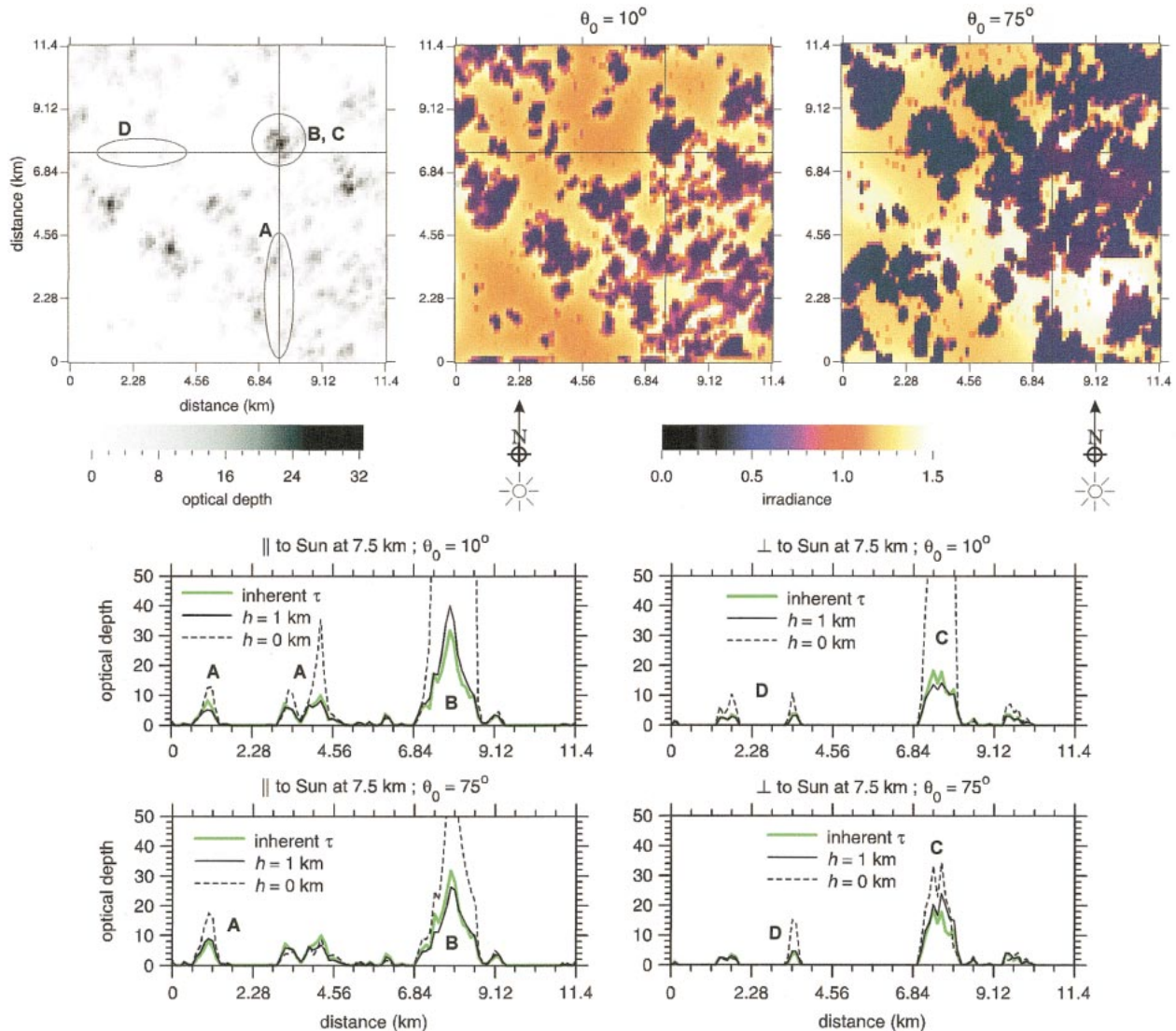


FIG. 10. (top)  $\tau$  for scene A (replot of Fig. 4) and surface irradiances for surface albedo of 0.5 at  $\theta_0 = 10^\circ$  and  $75^\circ$ . (bottom) Transects of inherent  $\tau$  and  $\tau$  inferred assuming  $h = 0$  km and 1 km along the two transects marked on (top). Alphabetically denoted regions marked on both the optical depth map and the plots are discussed in the text.

sumed to be homogeneous and Lambertian. Although radiances and fluxes were generated for  $\alpha_\lambda$  from 0 to 0.9 in increments of 0.1, results focus on  $\alpha_1 = 0.1$  and  $\alpha_2 = 0.5$  (cf. Table 1).

The method is illustrated for two  $(11.4 \text{ km})^2$  fields of shallow marine boundary layer clouds whose optical depths were inferred from 28.5-m resolution Landsat imagery assuming a droplet effective radius of  $10 \mu\text{m}$  (Harshvardhan et al. 1994). To reduce computational burden, the fields were degraded to  $\Delta x = 114 \text{ m}$ . This altered them minimally as radiative smoothing (Marshak et al. 1995) had already eliminated much variability less than  $\sim 100 \text{ m}$ .

Figure 4 shows that scene A consists of numerous clouds with areas less than  $2 \text{ km}^2$  and scene B is dominated by a few clouds with areas near  $10\text{--}30 \text{ km}^2$ . Table

2 summarizes key features of the fields. All cloud-base altitudes  $h$  for scene A were 1 km while those for scene B were 0.5 km. Cloud geometric thicknesses (in meters) were dictated by

$$z_c = 45.2\tau^{2/3}, \quad (15)$$

which approximates the empirical relation reported by Minnis et al. (1992). Cloud in each column was assumed to be horizontally and vertically homogeneous. Vertical resolution was 50 m. To make clouds in scene A resemble clouds over land (smaller drops), retrieved extinction coefficients were multiplied by 2.

#### 4. Results

All simulations reported here used  $\theta_0$  of either  $10^\circ$ ,  $30^\circ$ ,  $60^\circ$ , or  $75^\circ$ , and  $\alpha_1 = 0.1$  and  $\alpha_2 = 0.5$ . Each

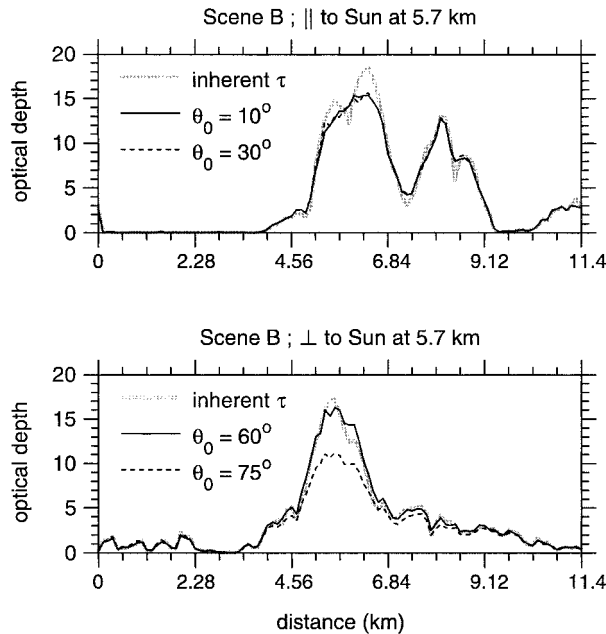


FIG. 11. Series of inherent  $\tau$  and  $\tau'$  for several  $\theta_0$  along transects that are (top) parallel to and (bottom) perpendicular to the Sun across the center (at 5.7 km) of scene B (see Fig. 4).

simulation received  $10^9$  photons or  $10^5$  photons per column. In all cases, the Sun shone from the south (see Fig. 4); other solar azimuth angles were tested and all yielded results similar to those presented. Retrievals were done along transects running vertically (parallel to the Sun) and horizontally (perpendicular to the Sun) across the fields in Fig. 4. In a crude fashion, this simulates wind from two directions and acknowledges that clouds usually exhibit some anisotropic structure (e.g., Schertzer and Lovejoy 1987). Also, all  $F_{\lambda}^{\uparrow}$  were computed using  $n = \text{INT}[(h/\Delta x) \tan 80^\circ]$  in (10) (i.e., out to an  $80^\circ$  nadir angle). Unless mentioned otherwise, retrievals were performed using correct values of  $h$ .

Figure 5 shows  $I_{\lambda}^{\downarrow}$  for scene A as a function of  $\tau$  for a black surface when columns are treated independently (1D transfer) in the Monte Carlo algorithm. There are sufficiently many samples that the scatter gives a graphical indication that Monte Carlo noise is  $\leq 0.02I_{\lambda}^{\downarrow}$ , which is comparable to, if not better than, most radiometers. Errors for irradiance are roughly 5 times smaller than those for radiance. Also shown in Fig. 5 are corresponding 3D results. Compared to the 1D results, the scatter of 3D points leaves no hope for simple mappings between  $I_{\lambda}^{\downarrow}$  and  $\tau$  like those used for  $F_{\lambda}^{\uparrow}$  and  $\tau$  during overcast conditions (e.g., Barker et al. 1998).

#### a. Retrievals for 3D clouds

Figure 6 shows a plot of  $\tau'$  against  $\tau$  for both scenes at two vastly different sun angles for points along all 100 transects parallel to the Sun. The log-log scale shows that relative variances of  $\tau'$  for a given  $\tau$  are

TABLE 2. Properties of the cloud fields shown in Fig. 4:  $\theta_{\text{obs}}$  is solar zenith angle at time of observation;  $A_c$  is vertically projected cloud fraction;  $\bar{\tau}$  and  $\tau_{\text{max}}$  are mean and maximum cloud optical depths;  $\nu \equiv (\bar{\tau})^2/\tau^2$ .

	$\theta_{\text{obs}}$	$A_c$	$\bar{\tau}$	$\tau_{\text{max}}$	$\nu$
Scene A	$33^\circ$	0.48	3.37	32.2	0.39
Scene B	$30^\circ$	0.88	2.68	19.2	0.39

almost independent of  $\tau$  and typically  $< 50\%$  (increasing slightly with  $\theta_0$ ). These plots also show that for scene A,  $\tau'$  tends to be overestimated for  $\tau \lesssim 5$  and underestimated for larger  $\tau$ . This is because within clouds, radiation tends to be channeled from dense to tenuous regions (e.g., Davis 1992; Barker and Li 1997). Having invoking the assumption of local 1D transfer, however, squelched the sink-source aspect of  $\mathcal{G}$  so the algorithm interprets positive net horizontal sources of photons as anomalous optical depth. That is, the cloud appears to be reflecting too much given the estimate of  $F_{\lambda}^{\uparrow}(j, z_{\text{base}})$ . Likewise, unaccounted for negative net horizontal sources, or sinks, are perceived as areas of overly weak reflectance and so  $\tau$  are underestimated. This is not so apparent for scene B because its clouds are fairly planar and thus produce weaker net horizontal fluxes than in scene A.

While direct comparisons such as in Fig. 6 are useful, particularly when  $\tau'$  are to be used in synergy with other data measured simultaneously, Barker et al. (1996) demonstrated that for domain sizes resembling those of global climate models, use of the first two moments of  $\tau$  in a modified two-stream approximation usually provide accurate estimates of domain-averaged radiative fluxes. Therefore, Fig. 7 shows frequency distributions of inherent  $\tau$  and  $\tau'$  for scenes A and B. Histograms represent results from all 100 transects parallel and perpendicular to the Sun. Distributions of  $\tau'$  are for the most part excellent renditions of those for  $\tau$  and are almost independent of  $\theta_0$ . This implies that series of estimated  $F_{\lambda}^{\uparrow}(j, z_{\text{base}})$  are often sufficient. When this is the case, the algorithm is well informed about the amount of radiation undergoing multiple reflections between surface and cloud. The only notable exception is that both scenes display minor tendencies to underestimate large  $\tau$  along transects perpendicular to the Sun. In the appendix it is shown that to obtain accurate  $\tau'$  at low sun, it is essential that irradiances be measured.

Table 3 summarizes mean  $\tau'$ , denoted as  $\bar{\tau}'$ , and  $\nu \equiv (\bar{\tau}')^2/(\bar{\tau})^2$ . Clearly these key parameters (Barker et al. 1996) are retrieved well when time series of radiances and irradiances are utilized. Most of the error is random as  $|\text{rmse}/\text{MBE}|$  typically exceed 15, though both types of errors are at least an order of magnitude larger than for ICA simulations and retrievals. As Fig. 6 shows, however, random error increases with  $\tau$ , but relative abundance decreases as shown in Fig. 7. Also, relative mean bias errors are typically less than 5% for these

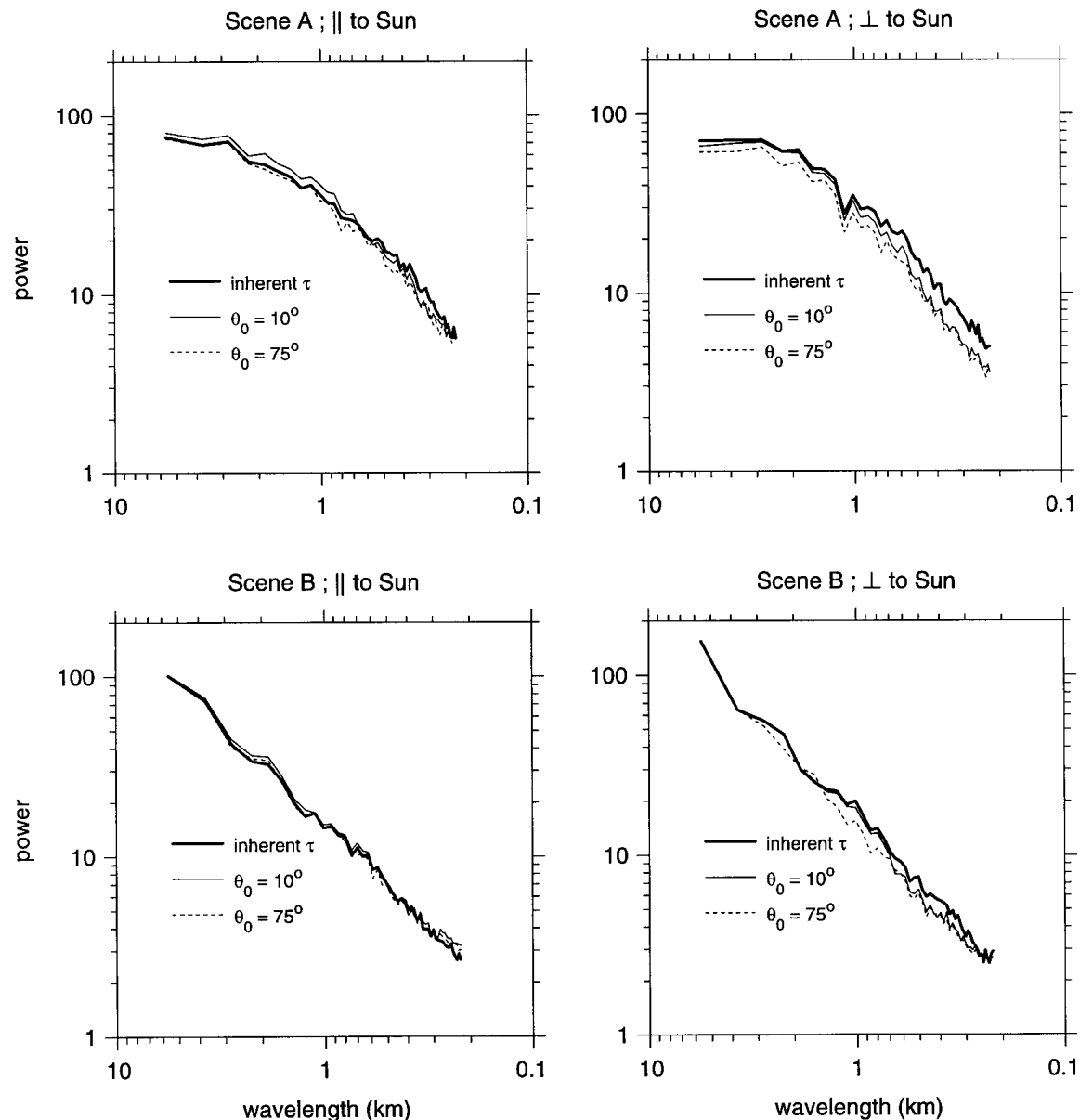


FIG. 12. (top) Ensemble-averaged 1D power spectra for inherent  $\tau$  and corresponding  $\tau'$  at  $\theta_0 = 10^\circ$  and  $75^\circ$  for transects parallel to (||) and perpendicular to ( $\perp$ ) the Sun across scene A. (bottom) Same as (top) except they are for scene B.

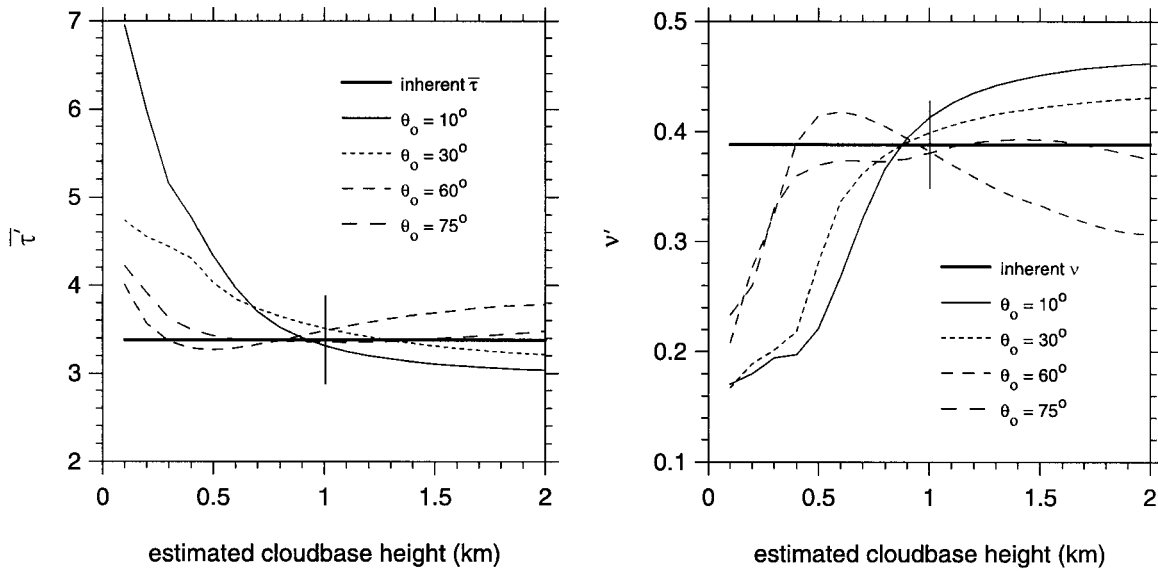
cases and transect orientation relative to the Sun is typically of modest to minor importance.

The excellent showings in Fig. 7 and Table 3 do not address the issue, faced by all fixed cloud observing systems, of how representative a single transect of  $\tau$  is to the field from which it was drawn (e.g., Barker 1996b; Astin and Di Girolamo 1999). Figure 8 shows cloud fraction as well as inherent and inferred  $\bar{\tau}$  and  $\nu$  for each transect across scene B at  $\theta_0 = 30^\circ$  (results for other  $\theta_0$  and scene A are similar). There are two main points to this figure. First, for such short transects, there is a large probability of randomly selecting a transect that does not represent the mean field well (see inherent

values in Table 2). Second, despite the often poor representativeness of each transect, the first two retrieved moments per transect are still extremely good (except near domain edges where the lack of cyclic clouds can lead to extreme and systematic horizontal transport and thus poor performance).

For reference, Fig. 9 shows frequency distributions of  $\tau'$  obtained when only point measurements of irradiance are used (e.g., Leontyeva and Stamnes 1994). As expected, irradiance by itself lacks sufficient information pertaining to high-frequency cloud structure and so distributions of  $\tau'$  are much in error. Errors for scene B are much smaller than those for scene A because its

Scene A ; || to Sun



Scene B ; || to Sun

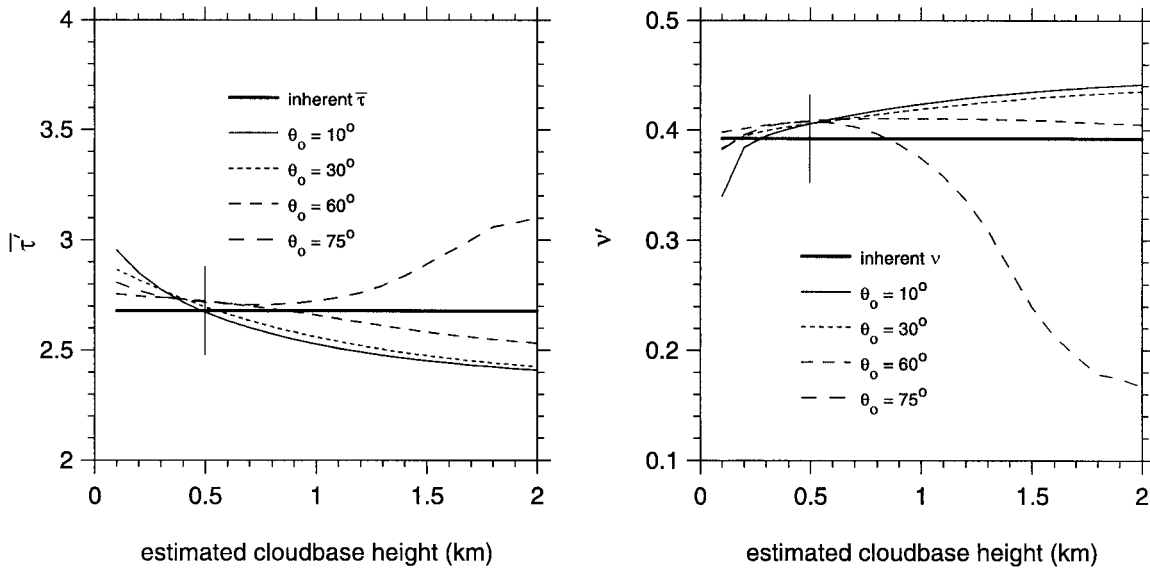


FIG. 13. (top) Mean inferred optical depth,  $\bar{\tau}$ , and  $v'$  as functions of estimated cloud-base altitude  $h'$  for transects parallel to the Sun across scene A for several  $\theta_0$ . Thick horizontal lines indicate inherent values. Thin vertical lines indicate true values of cloud-base altitude (as used in the Monte Carlo simulations). (bottom) Same as (top) except they are for scene B.

clouds are relatively planar. Time-averaging irradiances (as is usually done with this method) would not help; it would only tighten the histograms around an improper (effective) mean with the impact of clear sky folded in.

Figure 10 highlights both the importance and the limitations of using irradiance time series from a single site

to estimate  $F_{\lambda}^{\uparrow}$ . It shows maps of  $\tau$  and normalized surface irradiance (transmittance) at  $\alpha = 0.5$  for scene A at  $\theta_0 = 10^\circ$  and  $75^\circ$ . Note that as  $\theta_0$  increases, cloud shadows merge and migrate north while regions of enhanced irradiance (cloud side scatter) expand but remain primarily beneath and just to the south of the largest

TABLE 3. Properties of the cloud fields shown in Fig. 4 and corresponding values retrieved with (12) and (14). The  $\theta_0$  is solar zenith angle,  $\bar{\tau}$  is mean cloud optical depth, and  $\nu \equiv (\bar{\tau})^2/\tau^2$ . Values inherent to the fields are in columns labeled “inherent  $\tau$ ”; values for transects parallel to ( $\parallel$ ) and perpendicular to ( $\perp$ ) the sun are labeled as such. Values in parentheses are mean bias errors (MBE) and root-mean-square errors (rmse) for estimated  $\tau$  ( $\tau_{\text{rmse}}^{\text{MBE}}$ ). Cloud detection threshold was  $I_{\lambda_2}^{\downarrow} > 0.001$ .

	Inherent $\tau$	$\theta_0 = 10^\circ$		$\theta_0 = 75^\circ$	
		Transects $\parallel$ to sun	Transects $\perp$ to sun	Transects $\parallel$ to sun	Transects $\perp$ to sun
Scene A					
$\bar{\tau}$	3.37	3.31 ( $^{-0.06}$ 1.20)	3.16 ( $^{-0.19}$ 1.26)	3.35 ( $^{-0.02}$ 2.09)	3.11 ( $^{-0.26}$ 1.54)
$\nu$	0.39	0.41	0.44	0.38	0.46
Scene B					
$\bar{\tau}$	2.68	2.67 ( $^{-0.01}$ 0.61)	2.67 ( $^{-0.01}$ 0.59)	2.72 ( $^{+0.04}$ 0.70)	2.68 ( $^{0.00}$ 0.85)
$\nu$	0.39	0.41	0.41	0.41	0.41

clouds. Two transects are marked on these maps and their series of  $\tau$  and corresponding inferences  $\tau'$  using  $h = 0$  and 1 km are shown on the four lower plots;  $h = 0$  affects  $F_{\lambda}^{\uparrow}(j, z_{\text{base}}) = \alpha_{\lambda} F_{\lambda}^{\downarrow}(j)$  in (10) [i.e.,  $w(k - j) = \delta_{kj}$ ]. Noteworthy errors are labeled on the map and graphs and are discussed here:

- A. At  $\theta_0 = 10^\circ$  and  $75^\circ$  with  $h = 1$  km, the algorithm had little difficulty with these thin clouds. However, when  $h = 0$  km, point irradiances were generally too low (radiometers were often in the shadow of the cloud in the zenith) and the algorithm was not informed of adjacent bright areas. As such, it was ill informed about the amount of radiation available to initiate multiple reflections, and so to account for the observed radiance difference [the numerator (12)] it made 1D clouds more reflective by inflating  $\tau'$ . But, as 1D clouds thicken and become more reflective they transmit less radiation to begin with so the gulf between  $\tau'$  and  $\tau$  can broaden rapidly depending on the extent to which the local field of  $\tau$  deviates from uniformity.
- B. As in A, when  $h = 0$  km, the amount of radiation initiating multiple reflections was underestimated so  $\tau'$  are too large. In fact, near the center of the clouds at B, the algorithm failed as

$$\rho_{\tau} = \frac{I_{\lambda_2}^{\downarrow}(j) - I_{\lambda_1}^{\downarrow}(j)}{F_{\lambda_2}^{\uparrow}(j, z_{\text{base}}) - F_{\lambda_1}^{\uparrow}(j, z_{\text{base}})} > 1, \quad (16)$$

which resulted in  $\tau'$  being set to the maximum value of 100. The same problem, but to a much lesser extent,

faced the algorithm when  $h = 1$  km and  $\theta_0 = 10^\circ$  with the transect parallel to the Sun for it too overestimated  $\tau$ . The crucial information lacking was the presence of clear areas  $< 300$  m to the east and west. This problem was diminished greatly at  $\theta_0 = 75^\circ$  and when the transect was perpendicular to the Sun (next point).

- C. Beneath the cloud at C, measured irradiances at  $\theta_0 = 10^\circ$  and  $75^\circ$  were almost equal but less than their respective local area averages. Thus, when  $h = 0$  km, the algorithm failed at  $\theta_0 = 10^\circ$  [for the same reason as in (16)], but did quite well at  $\theta_0 = 75^\circ$ . For  $h = 1$  km, it displays minor tendencies to underestimate on the west for  $\theta_0 = 10^\circ$  and overestimate on the east for  $\theta_0 = 75^\circ$ . In the former case, the importance of the cloud shadow to the north was not captured, while in the latter, the extremely bright area immediately to the north was missed almost entirely.
- D. The source of the errors for  $h = 0$  km as seen here is the same as those for A, B, and C: underestimation of radiation involved in multiple reflections. Again, however, when  $h = 1$  km the algorithm had no difficulty estimating  $\tau$ .

Figure 11 shows examples of transects running both ways across the center of scene B (see Fig. 4). Near the 7-km mark for the  $10^\circ$  and  $30^\circ$  transects, horizontal leakage of photons from the local maxima into the intervening local minimum probably explains the negative and positive biases in  $\tau'$ . For the transect perpendicular to the sun at  $\theta_0 = 75^\circ$ , the algorithm underestimated  $\tau$  substantially through the thickest portion of the cloud. This

TABLE 4. Mean cloud optical depth  $\bar{\tau}$  and  $\nu \equiv (\bar{\tau})^2/\tau^2$  inherent to both scenes and inferred at various solar zenith angles  $\theta_0$  when arithmetic mean surface irradiance along a transect is used to estimate  $F^{\uparrow}$  at cloud base. This is tantamount to setting cloud-base altitude  $h$  in (11b) very large. Values inherent to the fields are in columns labeled “inherent  $\tau$ .” For the inferred quantities, values on the left are for transects parallel to the Sun while those on the right are for transects perpendicular to the Sun.

	Inherent $\tau$	$\theta_0$			
		$10^\circ$	$30^\circ$	$60^\circ$	$75^\circ$
Scene A					
$\bar{\tau}$	3.37	3.08/3.02	3.15/3.02	3.50/3.42	3.63/3.16
$\nu$	0.39	0.45/0.46	0.44/0.45	0.37/0.29	0.34/0.43
Scene B					
$\bar{\tau}$	2.68	2.37/2.43	2.37/2.43	2.44/2.54	3.30/2.72
$\nu$	0.39	0.45/0.45	0.44/0.45	0.40/0.42	0.14/0.40

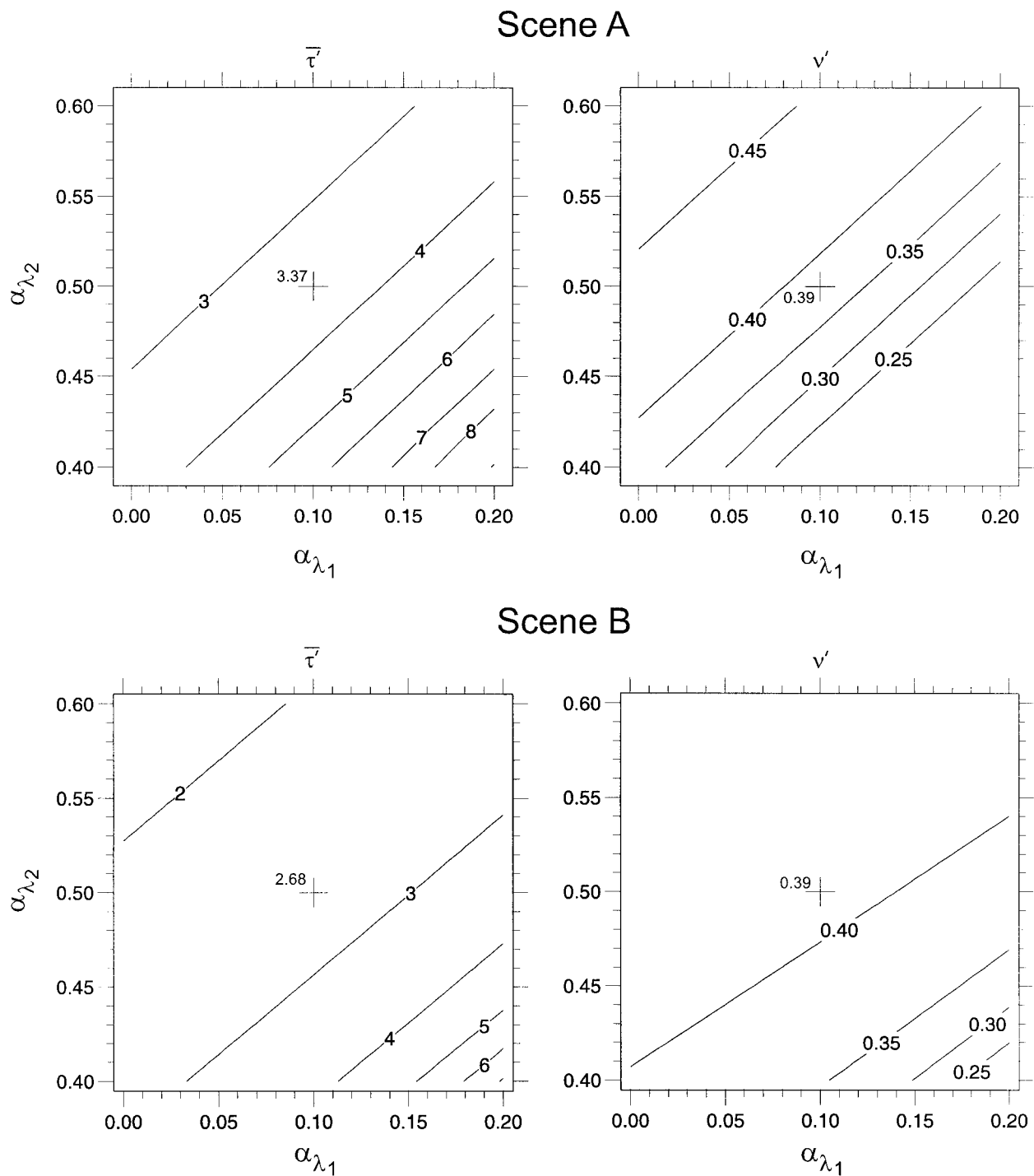


FIG. 14. (top) Contour plots of  $\bar{\tau}$  and  $\nu'$  for transects parallel to the Sun across scene A with  $h = 1$  km and  $\theta_0 = 60^\circ$ . Values of  $\alpha_{\lambda_1}$  and  $\alpha_{\lambda_2}$  listed along the axes were used in (10) though the true values, that set  $I^\downarrow$  and  $F^\downarrow$  in (12), were 0.1 and 0.5 (the crosses at the centers of the plots). Inherent values of mean  $\tau$  and  $\nu$  are listed on the plots. (bottom) Same as (top) except they are for scene B using  $h = 0.5$  km.

is because irradiance measured along the transect was in full direct sun (which undercut the cloud) while just to the north was cloud shadow. As such, the algorithm overestimated the amount of radiation involved in multiple reflections and thus required too little optical depth to

account for the difference in the numerator of (12). On the contrary, the  $60^\circ$  transect sampled the irradiance field well and estimation of  $\tau$  was almost perfect; though there is evidence of minor horizontal transport effects as just discussed for the  $10^\circ$  and  $30^\circ$  transects.

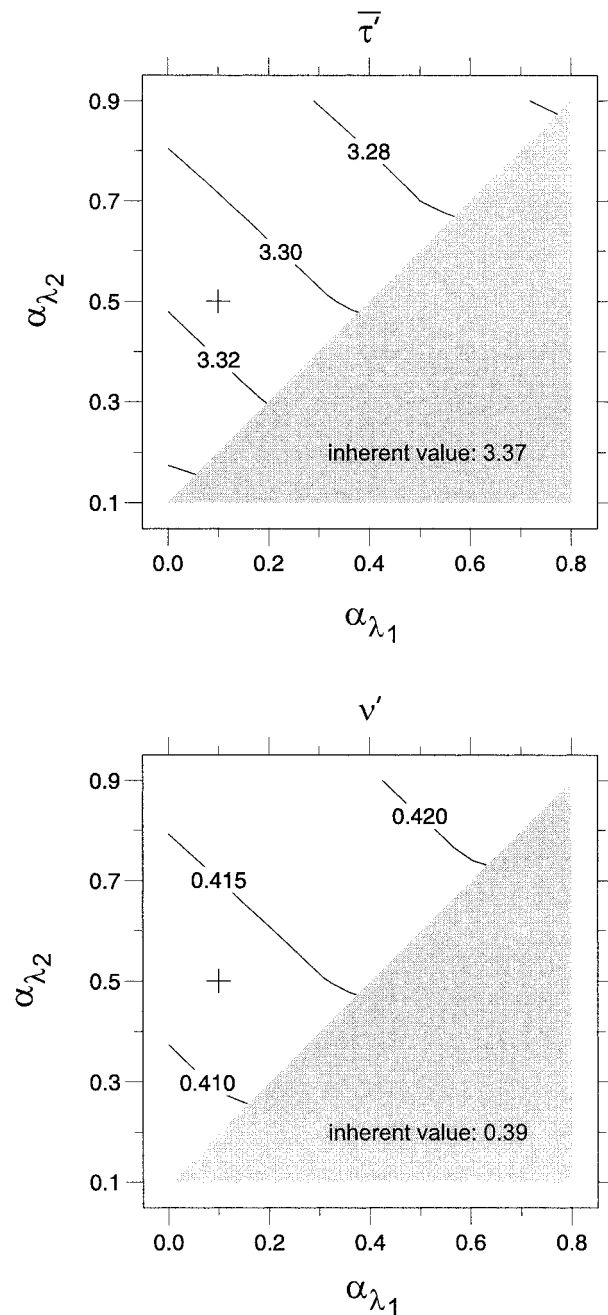


FIG. 15. Contour plots of  $\bar{\tau}'$  and  $\nu'$  for transects parallel to the Sun across scene A using  $h = 1$  km,  $\theta_0 = 60^\circ$ , and  $I^\downarrow$  and  $F^\downarrow$  in (12) corresponding to surface albedos listed on the axes. Region of admissible values is defined by  $\alpha_{\lambda_1} < \alpha_{\lambda_2}$ . Inherent values are listed on the plots. Crosses mark conditions used in all other experiments reported in this paper ( $\alpha_{\lambda_1} = 0.1$  and  $\alpha_{\lambda_2} = 0.5$ ).

Figure 12 shows ensemble-averaged 1D power spectra of  $\tau$  and  $\tau'$  for scenes A and B. By most accounts, spectra of  $\tau'$  are excellent renditions of spectra for inherent  $\tau$  regardless of advection direction and  $\theta_0$ . As shown in the appendix, when only radiances are used, spectra of  $\tau'$  are excellent for small  $\theta_0$  but become rather

poor at large  $\theta_0$ . This is because surface irradiance patterns often have little to do with cloud fluctuations in a narrow FOV near the zenith, particularly at high frequencies for transects perpendicular to the sun (cf. Zuidema and Evans 1998).

#### b. Errors due to estimation of cloud-base altitude

Estimates of  $F_\lambda^\uparrow(j, z_{\text{base}})$  depend, in part, on estimated cloud-base altitude  $h'$ . Figure 13 shows  $\bar{\tau}'$  and  $\nu'$  as functions of  $h'$  for transects parallel to the Sun across scenes A and B. For scene A,  $\bar{\tau}'$  and  $\nu'$  depend weakly on  $h'$  when  $h'$  is near, or greater than, the true value of  $h = 1$  km. This is because  $F_\lambda^\uparrow$  as computed by (10) asymptotes fairly rapidly for small scattered clouds. When  $h'$  seriously underestimates  $h$  in conjunction with small  $\theta_0$ , excessive values of  $\tau'$  occur at times (typically beneath thick clouds) thereby broadening the distribution of  $\tau'$  and reducing  $\nu'$ . For reasons explained earlier, this overestimation becomes catastrophic as  $h' \rightarrow 0$ . At large  $\theta_0$ , however, these types of errors occur less often and so estimates of  $\tau'$  are less sensitive to error in  $h$ . Since scene B's clouds are more planar than scene A's, its  $\tau'$  are typically much less sensitive to errors in  $h$ . It is encouraging to see that for both scenes, estimates of  $\bar{\tau}'$  and  $\nu'$  for different  $\theta_0$  tend to converge for  $h'$  near its proper value.

Table 4 lists values of  $\bar{\tau}'$  and  $\nu'$  for scene A and B when simple arithmetic means of  $F_\lambda^\downarrow$  [affected by letting  $h \rightarrow \infty$  in (11b)] along each transect are used to estimate  $F_\lambda^\uparrow$ . This simplification does not pose much of a problem for scene A due to high-frequency fluctuations in  $F_\lambda^\downarrow$  stemming from small broken clouds; results are almost as good as those listed in Table 3. For scene B, however, the relative impact is larger and results tend to be substantially worse than in Table 3. Values of  $\bar{\tau}'$  are too small because estimates of  $F_\lambda^\uparrow$  beneath clouds are too large (the more so the larger  $\tau$ ); particularly for small  $\theta_0$  where too much influence is given to regions of high irradiance far from cloud shadows.

#### c. Errors due to estimation of surface albedos

An obvious question for this method (and any other method that retrieves  $\tau$ ) is: given that estimates of surface albedos are effective values for the vicinity around an observation site, how sensitive are  $\tau'$  to errors in surface albedo? There are two ways to address this. First, recognizing that all surfaces are inhomogeneous, how important are fluctuations in surface albedo assuming  $\alpha_{\lambda_1}$  and  $\alpha_{\lambda_2}$  are estimated well? Second, if the surface shows little variability or high frequency variability over short ranges such that the homogeneous assumption is sufficient (e.g., Wiscombe et al. 2000), how important are good estimates of  $\alpha_{\lambda_1}$  and  $\alpha_{\lambda_2}$ ? Given the nature of the simulations performed here, only the second type of error can be explored for now.

The impact on  $\tau'$  due to errors in  $\alpha_{\lambda_1}$  and  $\alpha_{\lambda_2}$  was

explored as follows. Values of  $I_{\lambda}^{\downarrow}$  and  $F_{\lambda}^{\downarrow}$  associated with what were deemed to be *correct* values of  $\alpha_{\lambda_1}$  and  $\alpha_{\lambda_2}$  were used in (10) and (12) along with  $\alpha_{\lambda_1} + \Delta\alpha_{\lambda_1}$  and  $\alpha_{\lambda_2} + \Delta\alpha_{\lambda_2}$ , where  $\Delta\alpha_{\lambda_1}$  and  $\Delta\alpha_{\lambda_2}$  are errors, in (10). These errors are illustrated for scenes A and B at  $\theta_0 = 60^\circ$  where the true values of  $\alpha_{\lambda_1}$  and  $\alpha_{\lambda_2}$  were assumed to be 0.1 and 0.5.

Figure 14 shows contour plots  $\overline{\tau'}$  and  $\nu'$  for  $\Delta\alpha_{\lambda_1}$  and  $\Delta\alpha_{\lambda_2}$  between  $\pm 0.1$ . The near diagonal contours indicate that as long as the difference  $\Delta\alpha_{\lambda_2} - \Delta\alpha_{\lambda_1}$  is small, the algorithm performs well. Furthermore, when  $\Delta\alpha_{\lambda_2} > 0$  and  $\Delta\alpha_{\lambda_1} < 0$ , errors in  $\tau'$  are not severe. The most detrimental errors involve  $\Delta\alpha_{\lambda_2} < 0$  coupled with  $\Delta\alpha_{\lambda_1} > 0$  for the algorithm underestimates multiple reflections in the bright band and makes up for it by overestimating  $\tau$ . This is evident in the plots of  $\nu'$ ; decreased values of  $\nu'$  indicate broadened distributions of  $\tau'$ . Similar results were obtained for other  $\theta_0$  and other values of  $\alpha_{\lambda_1}$  and  $\alpha_{\lambda_2}$ .

## 5. Summary and conclusions

The purpose of this paper was to introduce and test a method of inferring cloud optical depth  $\tau$  for realistic broken clouds. Motivated by Marshak et al.'s (2000) NDCI method, this method uses time series of solar spectral zenith radiances and irradiances measured at the surface and relies on spectrally diverse area-averaged surface albedos. The inversion algorithm is simple for it is based on the same assumption made for virtually all other retrieval schemes: that localized radiative transfer in clouds can be modeled approximately by 1D theory. Its primary requirement is cloudbase irradiance at the zenith point which is estimated from time series of measured surface irradiance  $F^{\downarrow}$  and the frozen turbulence assumption. A method for use when only radiances are measured is presented in the appendix. The algorithm was tested using simulated surface measurements for two wavelengths generated by a 3D Monte Carlo algorithm operating on two fields of  $\tau$ . As these fields contain numerous small finite clouds and are quite inhomogeneous, this method was subject to stringent tests.

Given the simplifications on which the algorithm is built, estimates of  $\tau$  are surprisingly accurate: typical relative mean bias errors are generally less than 5%. This accuracy for the mean is almost independent of  $\theta_0$  but depends somewhat on estimates of cloudbase altitude  $h$  (preferably erring on the high side), cloud advection rate, and the two spectral surface albedos. When estimates of cloud-base irradiance are based only on instantaneous  $F^{\downarrow}$  (tantamount to setting  $h$  to zero), errors in inferred  $\tau$  can become catastrophic. If, on the other hand,  $h$  or cloud advection rate cannot be estimated, simple arithmetic mean  $F^{\downarrow}$ , over a reasonable window of time, could be used with greatest reliability for small broken clouds. It was demonstrated that errors in estimated local area-averaged surface albedos can be ex-

pected to degrade performance. The worst errors are those that reduce the difference between the two true albedos; the least damaging are those that overestimate the difference. On the other hand, as long as the *difference* in estimated albedos is accurate, inferred  $\tau$  should be accurate too. Like all fixed surface cloud observing systems, this method is at the mercy of advection and sampling. As such, one can never hope to entirely eliminate random error.

The method presented here goes well beyond the conventional approach of using  $F^{\downarrow}$  only. First, the conventional method is expected to work well only for overcast clouds; application to broken clouds was shown to be, understandably, disastrous. Second, during overcast conditions conventional estimates of  $\tau$  are *effective* values applicable to the pyranometer's field of view. The new method should have little difficulty yielding high-resolution time series of  $\tau$  for overcasts.

Results were shown only for surfaces that resemble green vegetation with  $\alpha_{\lambda_1} = 0.1$  and  $\alpha_{\lambda_2} = 0.5$ . This was because measurement signal-to-noise ratios and the differences in (12) will be large. In principle, however, this method works equally well for any  $\alpha_{\lambda_1} < \alpha_{\lambda_2}$  and  $\alpha_{\lambda_2} - \alpha_{\lambda_1}$  at least as small as 0.1. To demonstrate this, Fig. 15 shows contour plots of  $\overline{\tau'}$  and  $\nu'$  for transects parallel to the Sun across scene A at  $\theta_0 = 10^\circ$  as a function of  $\alpha_{\lambda_1}$  and  $\alpha_{\lambda_2}$  assuming they are estimated perfectly. This shows that retrieved  $\tau$  are almost independent of  $\alpha_{\lambda_1}$  and  $\alpha_{\lambda_2}$ , which expands the algorithm's range of application beyond green vegetated surfaces. The complication may be finding suitable narrow wave bands and achieving sufficiently large measurement signal-to-noise ratios when  $\alpha_{\lambda_2} - \alpha_{\lambda_1}$  are small.

Many deserving practical issues that will affect retrievals of  $\tau$  were either avoided or explored insufficiently in these exploratory experiments. For example, the impact of aerosols and Rayleigh scatter, excessive surface variability and bidirectionality, spatial variability of cloud droplet size distributions and phase, multilayered cloud systems, additional spectral channels, time averaging, and multiple surface sites are largely unexplored. Nevertheless, the excellent performance of this algorithm is encouraging for it should not only improve retrieval of  $\tau$  during overcast conditions, but also provide reliable retrievals for broken clouds.

*Acknowledgments.* HB and AM were supported by the U.S. Department of Energy under the respective Grants DE-FG02-90ER61071 (to E. E. Clothiaux at Penn State University) and DE-A105-90ER61069 (to NASA GSFC) as part of the ARM Program. AM was also supported by NASA's EOS Project Science Office at GSFC (under Grant NAG5-6675) as part of the EOS Validation Program. Thanks to B. Wielicki for making computer time available; Yu. Knyazikhin, A. Davis, and C. Pavloski for discussions; and W. Wiscombe for support. Extremely useful comments and suggestions were provided by two anonymous reviewers.

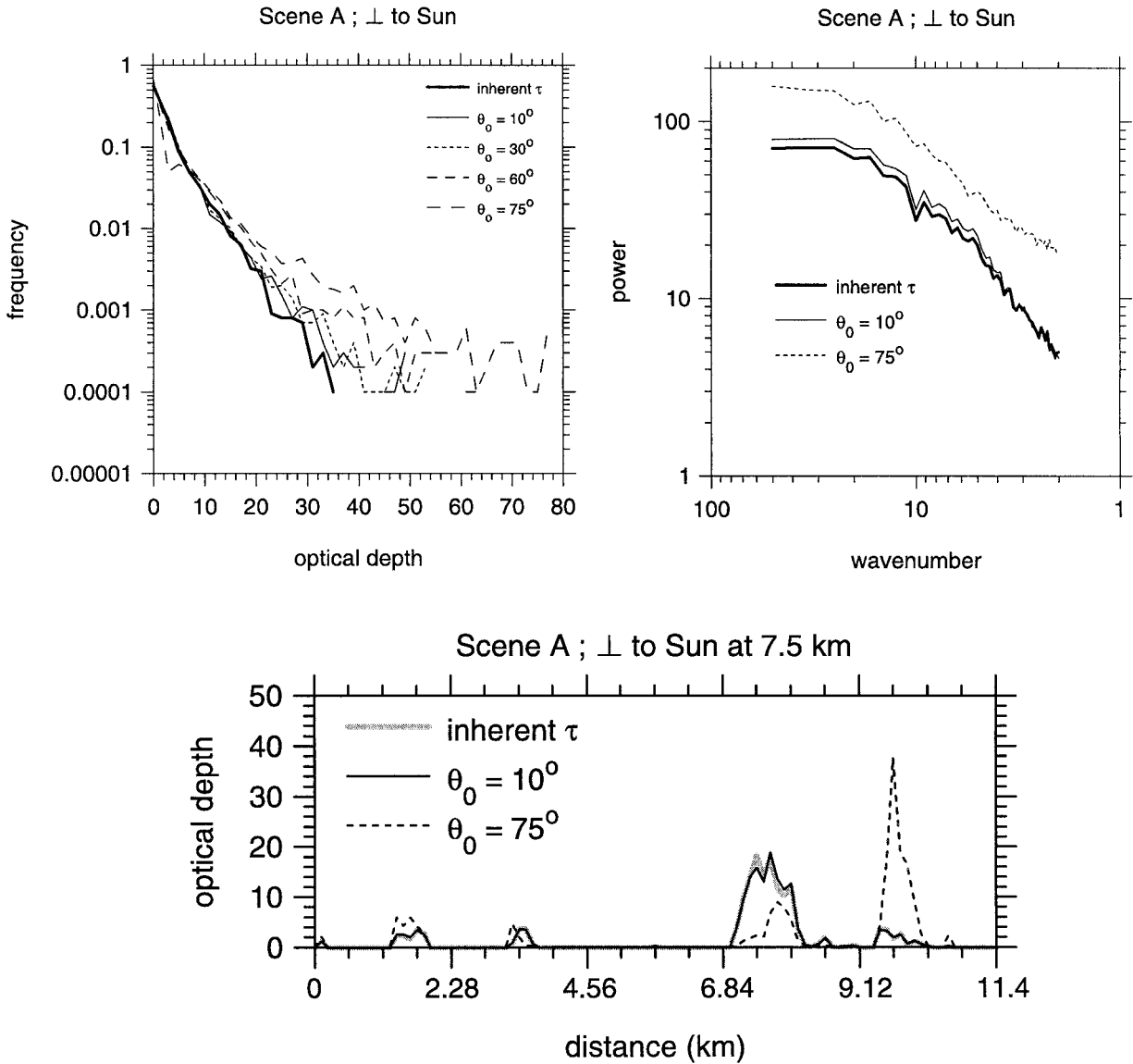


FIG. A1. (top left) Frequency distributions of inherent  $\tau$  and  $\tau'$  for several values of  $\theta_0$  for transects parallel to the Sun across A. These values of  $\tau'$  were inferred with the method documented in the appendix. (top right) Same as upper left except these are ensemble-average 1D power spectra for inherent  $\tau$  and  $\tau'$  for two values of  $\theta_0$ . (bottom) Time series of inherent  $\tau$  and  $\tau'$  for two values of  $\theta_0$  along the 7.5-km transect perpendicular to the Sun in A (cf. Fig. 10).

APPENDIX

**Inferring  $\tau$  When Only Nadir Radiances Are Measured**

This index is similar to Marshak et al.'s (2000) and is defined as

$$\mathcal{N} \equiv \frac{I_{\lambda_2}^\downarrow - I_{\lambda_1}^\downarrow}{I_{\lambda_1}^\downarrow}. \tag{A1}$$

Substituting (4) into (A1) yields

$$\mathcal{N} = \frac{\rho_\tau(F_{\lambda_2}^\uparrow - F_{\lambda_1}^\uparrow)}{I^0 + F_{\lambda_1}^\uparrow \rho_\tau}. \tag{A2}$$

The problem of estimating  $F_\lambda^\uparrow$  is made very difficult without measured irradiances. Nevertheless, assume, in the conventional 1D sense, that

$$F_\lambda^\uparrow = \frac{\alpha_\lambda T}{1 - \alpha_\lambda r}, \tag{A3}$$

where  $T$  and  $r$  are local area-averaged values of all-sky transmittance to downwelling direct beam, and all-sky

reflectance to upwelling diffuse beam, respectively. Substituting (A3) into (A2) yields

$$\mathcal{N} = \frac{T\rho_\tau(\alpha_{\lambda_2} - \alpha_{\lambda_1})}{(1 - \alpha_{\lambda_2}r)[I^0(1 - \alpha_{\lambda_1}r) + T\rho_\tau\alpha_{\lambda_1}]}. \quad (\text{A4})$$

Now, approximate  $T$  and  $r$  as

$$T \approx (1 - \langle A_c \rangle) + \langle A_c \rangle T_\tau, \quad \text{and} \quad (\text{A5a})$$

$$r \approx \langle A_c \rangle r_\tau, \quad (\text{A5b})$$

where  $T_\tau$  and  $r_\tau$  are 1D cloud transmittance for collimated irradiance incident at  $\theta_0$  and spherical albedo; both computed by DISORT. Here  $\langle A_c \rangle$  is a local area-averaged, vertically projected cloud fraction that can be defined using the time series of  $I_{\lambda_1}^\downarrow$  as

$$\langle A_c(j) \rangle = \begin{cases} \frac{\sum_{k=j-n}^{j+n} w(k-j)\Phi[I_{\lambda_1}^\downarrow(k)]}{\sum_{k=j-n}^{j+n} w(k-j)}; & I_{\lambda_1}^\downarrow(k) > 0 \\ 0; & I_{\lambda_1}^\downarrow(k) = 0, \end{cases} \quad (\text{A6a})$$

where

$$\Phi[x] = \begin{cases} 1; & x > 0 \\ 0; & x = 0, \end{cases} \quad (\text{A6b})$$

and the weighting function  $w$  is defined as in (11a). This definition of  $\Phi$  is tailored for the simulations used here:  $I_{\lambda_1}^\downarrow > 0$  implies cloud in the zenith. Spectral radiance reversal, as shown by Wiscombe et al. (2000), could also be used if one had measurements near  $0.4 \mu\text{m}$ .

Assume now that  $I^0$ ,  $\rho$ ,  $T_\tau$ , and  $r_\tau$  are local quantities that can be computed by DISORT and substituted into (A4). Then, a root-finding technique is applied to solve for  $\tau'$  (note that  $\mathcal{N}(\tau)$  can have a minimum at small  $\tau$ ). Fitting by Padé approximants [similar to (14)] were used here.

Figure A1 gives a brief impression of the performance of this algorithm for transects perpendicular to the Sun for scene A. For small  $\theta_0$ , time series, frequency distributions, and power spectra of  $\tau'$  are excellent and comparable to, and at times better than, those for the method documented in the main text. As  $\theta_0$  increases, however, cloud in the zenith, which is all this algorithm is informed of, can become completely irrelevant for estimating series of  $F_{\lambda_1}^\uparrow$ . As such, retrieved  $\tau$  are often much too large because the most damaging errors involve underestimation of  $F_{\lambda_1}^\uparrow$ . This is evident in both the histograms and time series in Fig. A1. Likewise, the power spectrum indicates far too much fluctuation in  $\tau'$  at all scales, again due largely to extreme overestimation of  $\tau$ .

#### REFERENCES

- Astin, I., and L. Di Girolamo, 1999: A general formalism for the distribution of the total length of a geophysical parameter along

a finite transect. *IEEE Trans. Geosci. Remote Sens.*, **37**, 508–512.

Barker, H. W., 1996a: A parameterization for computing grid-averaged solar fluxes for inhomogeneous marine boundary layer clouds. Part I: Methodology and homogeneous biases. *J. Atmos. Sci.*, **53**, 2289–2303.

—, 1996b: Estimating cloud field albedo using one-dimensional series of optical depth. *J. Atmos. Sci.*, **53**, 2826–2837.

—, and Z. Li, 1997: Interpreting shortwave albedo-transmittance plots: True or apparent anomalous absorption. *Geophys. Res. Lett.*, **24**, 2023–2026.

—, B. A. Wielicki, and L. Parker, 1996: A parameterization for computing grid-averaged solar fluxes for inhomogeneous marine boundary layer clouds. Part II: Validation using satellite data. *J. Atmos. Sci.*, **53**, 2304–2316.

—, T. J. Curtis, E. Leontieva, and K. Stamnes, 1998: Optical depth of overcast cloud across Canada: Estimates based on surface pyranometer and satellite measurements. *J. Climate*, **11**, 2980–2994.

Box, M. A., S. A. W. Gerstl, and C. Simmer, 1988: Application of the adjoint formulation of the calculation of atmospheric radiative effects. *Beitr. Phys. Atmos.*, **61**, 303–311.

Cahalan, R. F., W. Ridgway, W. J. Wiscombe, S. Gollmer, and Harshvardhan, 1994: Independent pixel and Monte Carlo estimates of stratocumulus albedo. *J. Atmos. Sci.*, **51**, 3776–3790.

Davis, A. B., 1992: Radiation transport in scale-invariant optical media. Ph.D. thesis, McGill University, 325 pp. [Available from McGill University, 47 Sherbrooke St. West, Montreal, QC H3A 3N6, Canada.]

—, A. Marshak, R. F. Cahalan, and W. J. Wiscombe, 1997: The Landsat scale break in stratocumulus as a three-dimensional radiative transfer effect: Implications for remote sensing. *J. Atmos. Sci.*, **54**, 241–260.

Han, Q., W. B. Rossow, J. Chou, and R. M. Welch, 1998: Global survey of the relationships of cloud albedo and liquid water path with droplet size using ISCCP. *J. Climate*, **11**, 1516–1528.

Harshvardhan, B. A. Wielicki, and K. M. Ginger, 1994: The interpretation of remotely sensed cloud properties from a model parameterization perspective. *J. Climate*, **7**, 1987–1998.

Heney, L. C., and J. L. Greenstein, 1941: Diffuse radiation in the galaxy. *Astrophys. J.*, **93**, 70–83.

Kimes, D. S., 1983: Dynamics of directional reflectance factor distributions for vegetation. *Appl. Opt.*, **22**, 1364–1372.

—, W. W. Newcomb, R. F. Nelson, and J. B. Schutt, 1986: Directional reflectance distribution of a hardwood and pine forest canopy. *IEEE Trans. Geosci. Remote Sens.*, **24**, 281–283.

Knyazikhin, Y., and A. Marshak, 2000: Mathematical aspects of BRDF modeling: Adjoint problem and Green's function. *Remote Sens. Rev.*, **18**, 263–280.

Leontieva, E., K. Stamnes, and J. A. Olseth, 1994: Cloud optical properties at Bergen (Norway) based on the analysis of long-term solar irradiance records. *Theor. Appl. Climatol.*, **50**, 73–82.

Leontieva, E., and K. Stamnes, 1994: Estimations of cloud optical thickness from ground-based measurements of incoming solar radiation in the Arctic. *J. Climate*, **7**, 566–578.

Li, Z., A. P. Trishchenko, H. W. Barker, G. L. Stephens, and P. Partain, 1999: Analyses of Atmospheric Radiation Measurement (ARM) program's Enhanced Shortwave Experiment (ARESE) multiple data sets for studying cloud absorption. *J. Geophys. Res.*, **104**, 19 127–19 134.

Lyapustin, A., 1999: Atmospheric and geometrical effects on land surface albedo. *J. Geophys. Res.*, **104**, 4127–4144.

Marchuk, G. I., G. A. Mikhailov, M. A. Nazoraliev, R. A. Dorbinjin, B. A. Kargin, and B. S. Elepov, 1980: *Monte Carlo Methods in Atmospheric Optics*. Series in Optical Sciences, Vol. 12, Springer-Verlag, 208 pp.

—, A. B. Davis, W. J. Wiscombe, and R. F. Cahalan, 1995: Radiative smoothing in fractal clouds. *J. Geophys. Res.*, **100**, 26 247–26 261.

- , L. Oreopoulos, A. B. Davis, W. J. Wiscombe, and R. F. Cahalan, 1999: Horizontal radiative fluxes in clouds and accuracy of the independent pixel approximation at absorbing wavelengths. *Geophys. Res. Lett.*, **26**, 1585–1588.
- , Y. Knyazikhin, A. B. Davis, W. J. Wiscombe, and P. Pilewskie, 2000: Cloud–vegetation interaction: Use of normalized difference cloud index for estimation of cloud optical thickness. *Geophys. Res. Lett.*, **27**, 1695–1698.
- Min, Q., and L. C. Harrison, 1996: Cloud properties derived from surface MFRSR measurements and comparison with GOES results at the ARM SGP site. *Geophys. Res. Lett.*, **23**, 1641–1644.
- Minnis, P., P. W. Heck, D. F. Young, C. W. Fairall, and J. B. Snider, 1992: Stratocumulus cloud properties from simultaneous satellite and island-based instrumentation during FIRE. *J. Appl. Meteor.*, **31**, 317–339.
- Myneni, R. B., and G. Asrar, 1993: Radiative transfer in three-dimensional atmosphere–vegetation media. *J. Quant. Spectrosc. Radiat. Transfer*, **49**, 585–598.
- Rossow, W. B., and R. A. Schiffer, 1991: ISCCP cloud products. *Bull. Amer. Meteor. Soc.*, **72**, 2–20.
- Schertzer, D., and S. Lovejoy, 1987: Physical modelling and analysis of rain and clouds by anisotropic scaling multiplicative processes. *J. Geophys. Res.*, **92**, 9693–9714.
- Stamnes, K., S.-C. Tsay, W. J. Wiscombe, and K. Jayaweera, 1988: A numerically stable algorithm for discrete-ordinate-method radiative transfer in multiple scattering and emitting layered media. *Appl. Opt.*, **27**, 2502–2509.
- Wiscombe, W. J., A. Marshak, Y. Knyazikhin, and A. B. Davis, 2000: The use of reflection from vegetation for estimating broken-cloud optical depth. *Proc. Tenth Atmospheric Radiation Measurement (ARM) Science Team Meeting*, San Antonio, TX, ARM Program. [Available online at <http://www.arm.gov>.]
- Zuidema, P., and K. F. Evans, 1998: On the validity of the independent pixel approximation for boundary layer clouds observed during ASTEX. *J. Geophys. Res.*, **103**, 6059–6074.